

WAVELET ALGORITHMS FOR HIGH-RESOLUTION IMAGE RECONSTRUCTION*

RAYMOND H. CHAN[†], TONY F. CHAN[‡], LIXIN SHEN[§], AND ZUOWEI SHEN[§]

Abstract. High-resolution image reconstruction refers to the reconstruction of high-resolution images from multiple low-resolution, shifted, degraded samples of a true image. In this paper, we analyze this problem from the wavelet point of view. By expressing the true image as a function in $\mathcal{L}(\mathbb{R}^2)$, we derive iterative algorithms which recover the function completely in the \mathcal{L} sense from the given low-resolution functions. These algorithms decompose the function obtained from the previous iteration into different frequency components in the wavelet transform domain and add them into the new iterate to improve the approximation. We apply wavelet (packet) thresholding methods to denoise the function obtained in the previous step before adding it into the new iterate. Our numerical results show that the reconstructed images from our wavelet algorithms are better than that from the Tikhonov least-squares approach. Extension to super-resolution image reconstruction, where some of the low-resolution images are missing, is also considered.

Key words. wavelet, high-resolution image reconstruction, Tikhonov least square method

AMS subject classifications. 42C40, 65T60, 68U10, 94A08

PII. S1064827500383123

1. Introduction. Many applications in image processing require deconvolving noisy data, for example the deblurring of astronomical images [11]. The main objective in this paper is to develop algorithms for these applications using a wavelet approach. We will concentrate on one such application, namely, the high-resolution image reconstruction problem. High-resolution images are often desired in many situations, but made impossible because of hardware limitations. Increasing the resolution by image processing techniques is therefore of great importance. The earliest formulation of the problem was proposed by Tsai and Huang [24] in 1984, motivated by the need of improved resolution images from Landsat image data. Kaltenbacher and Hardie [14], and Kim, Bose, and Valenzuela [15] applied the work of [24] to noisy and blurred images, using least-squares minimization. The high-resolution image reconstruction also can be obtained by mapping several low-resolution images onto a single high-resolution image plane, then interpolating it between the nonuniformly spaced samples [3, 23]. The high-resolution image reconstruction can also be put into a Bayesian framework by using a Huber–Markov random field; see, for example, Schultz and Stevenson [22].

Here we follow the approach in Bose and Boo [1] and consider creating high-resolution images of a scene from the low-resolution images of the same scene. When

*Received by the editors December 21, 2000; accepted for publication (in revised form) June 28, 2002; published electronically February 27, 2003.

<http://www.siam.org/journals/sisc/24-4/38312.html>

[†]Department of Mathematics, Chinese University of Hong Kong, Shatin, NT, People's Republic of China (rchan@math.cuhk.edu.hk). This author's research was supported in part by HKRGC grant CUHK4212/99P and CUHK Grant DAG 2060183.

[‡]Department of Mathematics, University of California, Los Angeles, Los Angeles, CA 90024-1555 (chan@math.ucla.edu). This author's research was supported in part by the ONR under contract N00014-96-1-0277 and by the NSF under grant DMS-9973341.

[§]Department of Mathematics, West Virginia University, Armstrong Hall, PO Box 6310, Morgantown, WV 26506 (lshen@math.wvu.edu, matzuows@math.nus.edu.sg). The research of these authors was supported in part by the Center of Wavelets, Approximation and Information Processing (CWAIP), funded by the National Science and Technology Board, the Ministry of Education under grant RP960 601/A.

we have a full set of low-resolution images, the problem is referred to as *high-resolution image reconstruction*; when only some of the low-resolution images are available, the problem is called *super-resolution image reconstruction*. In both cases, the low-resolution images are obtained from sensor arrays which are shifted from each other with subpixel displacements. The reconstruction of the high-resolution image can be modeled as solving a linear system $L\mathbf{f} = \mathbf{g}$, where L is the convolution operator, \mathbf{g} is a vector formed from the low-resolution images, and \mathbf{f} is the desired high-resolution image; see [1].

In this paper, we look at this problem from the wavelet point of view and analyze the process through multiresolution analysis. The true image can be considered as a function f in $\mathcal{L}_2(\mathbb{R}^2)$ and the low-resolution images can be thought of as the low-frequency samples of f obtained by passing f through some lowpass filters. Thus the problem can be posed as reconstructing a function from the given multiple low-frequency samples of f . To recover f , we iteratively deconvolve the high-frequency components of f which are hidden in the low-frequency samples. Our iterative process decomposes the function obtained in the previous iteration into different frequency components in the wavelet transform domain and then adds them to the new iterate to improve the approximation. In this setting, it is easy to apply wavelet methods to denoise the function obtained in the previous step before adding it into the new iterate.

The high-resolution image reconstruction problem is closely related to the deconvolution problem. In the recent works of [12] and [13], an analysis of minimizing the maximum risk over all the signals in a set of signals is given. Then, it was applied to estimate the risk of the wavelet thresholding method used on the deconvoluted signals. Their wavelet thresholding algorithm is proven to be close to the optimal risk bound when a mirror wavelet basis is used. The main difficulty in denoising deconvoluted signals is that when the convolution lowpass filter has zeros at high frequency, the noise variance in the solution has a hyperbolic growth [12]. To overcome this difficulty, a mirror wavelet basis is constructed to define a sparse representation of all the signals in the set of given signals and to nearly diagonalize the covariance operator of the noise in the deconvoluted solution in order to reach the optimal risk bound.

The approach here is different. The highpass filters are added to perturb the zeros of the convolution kernel to prevent the noise variance from blowing up. Our wavelet (packet) thresholding method, which is a wavelet denoising method, is built into each iterative step so as to remove the noise from the original data. It also keeps the features of the original signal while denoising. In this sense, our method is more related to the Tikhonov least-squares method [8], where a regularization operator is used to perturb the zeros of the convolution kernel and a penalty parameter is used to damp the high-frequency components for denoising. Since the least-squares method penalizes the high-frequency components of the original signal at the same rate as that of the noise, it smoothes the original signal. In contrast, our thresholding method penalizes the high-frequency components of the signal in a rate significantly lower than that of the noise, and hence it will not smooth the original signal in general. Moreover, there is no need to estimate the regularization parameter in our method. Our numerical tests show that the reconstructed images are of better quality. Also, our algorithms can easily be extended to the super-resolution case.

The outline of the paper is as follows. In section 2, we give a mathematical model of the high-resolution image reconstruction problem. In section 3, we derive our algorithms. Extensions to the super-resolution case are also discussed there. Numerical

examples are given in section 4 to illustrate the effectiveness of the algorithms. After the concluding remarks, we provide in the appendix an analysis of our algorithms via the multiresolution analysis.

2. The mathematical model. Here we give a brief introduction to the mathematical model of the high-resolution image reconstruction problem. Details can be found in [1]. Suppose the image of a given scene can be obtained from sensors with $N_1 \times N_2$ pixels. Let the actual length and width of each pixel be T_1 and T_2 , respectively. We will call these sensors *low-resolution sensors*. The scene we are interested in, i.e., the *region of interest*, can be described as

$$\mathbf{S} = \{(x_1, x_2) \in \mathbb{R}^2 \mid 0 \leq x_1 \leq T_1 N_1, 0 \leq x_2 \leq T_2 N_2\}.$$

Our aim is to construct a higher-resolution image of the same scene by using an array of $K_1 \times K_2$ low-resolution sensors. More precisely, we want to create an image of \mathbf{S} with $M_1 \times M_2$ pixels, where $M_1 = K_1 N_1$ and $M_2 = K_2 N_2$. Thus the length and width of each of these *high-resolution pixels* will be T_1/K_1 and T_2/K_2 , respectively. To maintain the aspect ratio of the reconstructed image, we consider only $K_1 = K_2 = K$.

Let $f(x_1, x_2)$ be the intensity of the scene at any point (x_1, x_2) in \mathbf{S} . By reconstructing the high-resolution image, we mean to find or approximate the values

$$\frac{K^2}{T_1 T_2} \int_{iT_1/K}^{(i+1)T_1/K} \int_{jT_2/K}^{(j+1)T_2/K} f(x_1, x_2) dx_1 dx_2, \quad 0 \leq i < M_1, 0 \leq j < M_2,$$

which is the average intensity of all the points inside the (i, j) th high-resolution pixel:

$$(1) \quad \left[i \frac{T_1}{K}, (i+1) \frac{T_1}{K} \right] \times \left[j \frac{T_2}{K}, (j+1) \frac{T_2}{K} \right], \quad 0 \leq i < M_1, 0 \leq j < M_2.$$

In order to have enough information to resolve the high-resolution image, there are subpixel displacements between the sensors in the sensor arrays. Ideally, the sensors should be shifted from each other by a value proportional to the length and the width of the high-resolution pixels. More precisely, for sensor (k_1, k_2) , $0 \leq k_1, k_2 < K$, its horizontal and vertical displacements $d_{k_1 k_2}^x$ and $d_{k_1 k_2}^y$ with respect to the point $(0, 0)$ are given by

$$d_{k_1 k_2}^x = \left(k_1 + \frac{1-K}{2} \right) \frac{T_1}{K} \quad \text{and} \quad d_{k_1 k_2}^y = \left(k_2 + \frac{1-K}{2} \right) \frac{T_2}{K}.$$

For this low-resolution sensor, the average intensity registered at its (n_1, n_2) th pixel is modeled by

$$(2) \quad g_{k_1 k_2}[n_1, n_2] = \frac{1}{T_1 T_2} \int_{T_1 n_1 + d_{k_1 k_2}^x}^{T_1 (n_1+1) + d_{k_1 k_2}^x} \int_{T_2 n_2 + d_{k_1 k_2}^y}^{T_2 (n_2+1) + d_{k_1 k_2}^y} f(x_1, x_2) dx_1 dx_2 + \eta_{k_1 k_2}[n_1, n_2].$$

Here $0 \leq n_1 < N_1$ and $0 \leq n_2 < N_2$ and $\eta_{k_1 k_2}[n_1, n_2]$ is the noise; see [1]. We remark that the integration is over an area the same size of a low-resolution pixel.

Notice that using the midpoint quadrature rule and neglecting the noise $\eta_{k_1 k_2}[n_1, n_2]$ for the moment,

$$\begin{aligned} g_{k_1 k_2}[n_1, n_2] &\approx f \left(T_1 \left(n_1 + \frac{1}{2} \right) + d_{k_1 k_2}^x, T_2 \left(n_2 + \frac{1}{2} \right) + d_{k_1 k_2}^y \right) \\ &= f \left(\frac{T_1}{K} \left(K n_1 + k_1 + \frac{1}{2} \right), \frac{T_2}{K} \left(K n_2 + k_2 + \frac{1}{2} \right) \right). \end{aligned}$$

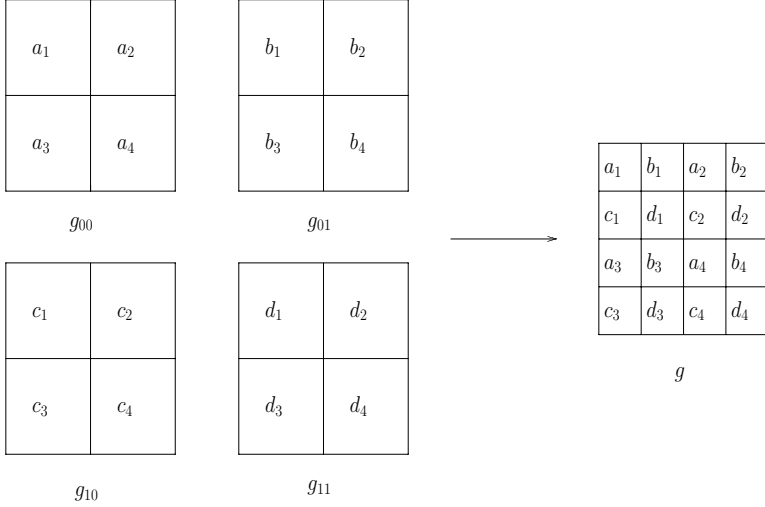


FIG. 1. Construction of the observed high-resolution image.

Thus, if we intersperse all the low-resolution images $g_{k_1 k_2}$ to form an $M_1 \times M_2$ image g by assigning

$$(3) \quad g[Kn_1 + k_1, Kn_2 + k_2] = g_{k_1 k_2}[n_1, n_2],$$

then

$$g[i, j] \approx f\left(\frac{T_1}{K}\left(i + \frac{1}{2}\right), \frac{T_2}{K}\left(j + \frac{1}{2}\right)\right), \quad 0 \leq i < M_1, 0 \leq j < M_2,$$

which is the value of f at the midpoint of the (i, j) th high-resolution pixel in (1). Thus g is an approximation of f . Figure 1 shows how to form a 4×4 image g from four 2×2 sensor arrays $\{g_{k_1 k_2}\}_{k_1, k_2=0}^1$, where all $g_{k_1 k_2}$ have 2×2 pixels. The image g , called the *observed high-resolution image*, is already a better image (i.e., better approximation of f) than any one of the low-resolution samples g_{k_1, k_2} themselves; see Figure 5(a)–(c) in section 4.

To obtain an image that is better than the observed high-resolution image g , one will have to solve (2) for f . According to [1], we solve it by first discretizing it using the rectangular quadrature rule. Or equivalently, we assume that for each (i, j) th high-resolution pixel given in (1), the intensity f is constant and is equal to $f[i, j]$ for every point in that pixel. Then carrying out the integration in (2), and using the reordering (3), we obtain a system of linear equations relating the unknown values $f[i, j]$ to the given low-resolution pixel values $g[i, j]$. This linear system, however, is not square. This is because the evaluation of $g_{k_1 k_2}[n_1, n_2]$ in (2) involves points outside the region of interest \mathbf{S} . For example, $g_{00}[0, 0]$ requires the values $f(x_1, x_2)$, where $x_1 < 0$ and $x_2 < 0$, i.e., it involves $f[-1, -1]$. Thus we have more unknowns than given values, and the system is underdetermined.

To compensate for this, one imposes boundary conditions on f for x_i outside the domain. A standard way is to assume that f is periodic outside:

$$f(x + iT_1 N_1, y + jT_2 N_2) = f(x, y), \quad i, j \in \mathbb{Z};$$

see, for instance, [9, section 5.1.3]. Other boundary conditions, such as the *symmetric* (also called Neumann or reflective) boundary condition and the *zero* boundary condition, can also be imposed; see [1, 18]. We emphasize that different boundary conditions will introduce different boundary artifacts in the recovered images. For example, compare Figure 5(d) with Figure 5(g) in section 4. For simplicity, we will only develop our algorithms for periodic boundary conditions here. For other boundary conditions, similar algorithms can be derived straightforwardly.

Using the periodic boundary condition and ordering the discretized values of f and g in a row-by-row fashion, we obtain an $M_1 M_2 \times M_1 M_2$ linear system of the form

$$(4) \quad L\mathbf{f} = \mathbf{g}.$$

The blurring matrix L can be written as

$$(5) \quad L = L^x \otimes L^y,$$

where \otimes is the Kronecker tensor product and L^x is the $M_1 \times M_1$ circulant matrix with the first row given by

$$\frac{1}{K} \left[1, \dots, 1, \frac{1}{2}, 0, \dots, 0, \frac{1}{2}, 1, \dots, 1 \right].$$

Here the first $K/2$ entries are equal to 1. We note that the last $K/2$ nonzero entries are there because of our periodic assumption on f . The $M_2 \times M_2$ blurring matrix L^y is defined similarly.

We note that the matrix L is a block-circulant-circulant-block (BCCB) matrix. Thus (4) can be solved by using three two-dimensional (2D) fast Fourier transforms (FFTs) in $O(M_1 M_2 \log(M_1 M_2))$ operations; see, for instance, [9, section 5.2.2]. As examples, the matrices L^x for the cases of 2×2 and 4×4 sensor arrays are given, respectively, by

$$(6) \quad L_2 \equiv \frac{1}{4} \begin{bmatrix} 2 & 1 & & 1 \\ 1 & 2 & 1 & \\ & \ddots & \ddots & \ddots \\ & & 1 & 2 & 1 \\ 1 & & 1 & 2 \end{bmatrix} \quad \text{and} \quad L_4 \equiv \frac{1}{8} \begin{bmatrix} 2 & 2 & 1 & & 1 & 2 \\ 2 & 2 & 2 & 1 & & 1 \\ 1 & 2 & 2 & 2 & 1 & \\ & \ddots & \ddots & \ddots & \ddots & \ddots \\ & & 1 & 2 & 2 & 2 & 1 \\ 1 & & & 1 & 2 & 2 & 2 \\ 2 & 1 & & & 1 & 2 & 2 \end{bmatrix}.$$

Because (2) is an averaging process, the system in (4) is ill-conditioned and susceptible to noise. To remedy this, one can use the Tikhonov regularization which solves the system

$$(7) \quad (L^* L + \beta R)\mathbf{f} = L^* \mathbf{g}.$$

Here R is a regularization operator (usually chosen to be the identity operator or some differential operators) and $\beta > 0$ is the regularization parameter; see [9, section 5.3]. If the boundary condition of R is chosen to be periodic, then (7) is still a BCCB system and hence can be solved by three FFTs in $O(M_1 M_2 \log(M_1 M_2))$ operations. If the symmetric boundary condition is used, then (7) is a block Toeplitz-plus-Hankel system with Toeplitz-plus-Hankel blocks. It can be solved by using three 2D fast cosine transforms (FCTs) in $O(M_1 M_2 \log(M_1 M_2))$ operations; see [18].

We note that (7) is derived from the least-squares approach of solving (4). In the next section, we will derive algorithms for finding \mathbf{f} by using the wavelet approach. They will improve the quality of the images when compared with (7).

3. Reconstruction. In this section, we analyze the model given in section 2 using the wavelet approach. Since (2) is an averaging process, the matrices in (6) can be considered as a lowpass filtering acting on the image \mathbf{f} with a tensor product refinement mask, say a . Let ϕ be the tensor product bivariate refinable function with such a refinement mask. Here, we recall that a function ϕ in $\mathcal{L}_2(\mathbb{R}^2)$ is *refinable* if it satisfies

$$\phi = 4 \sum_{\alpha \in \mathbb{Z}^2} a(\alpha) \phi(2 \cdot - \alpha).$$

The refinable function ϕ is also known as a scaling function. The sequence a is called a *refinement mask* (also known as a lowpass filter or a scaling coefficient). The *symbol* of the sequence a is defined as

$$\hat{a}(\omega) := \sum_{\alpha \in \mathbb{Z}^2} a(\alpha) e^{-i\alpha\omega}.$$

The function ϕ is *stable* if its shifts (integer translates) form a *Riesz system*, i.e., there exist constants $0 < c \leq C < \infty$, such that for any sequence $q \in \ell_2(\mathbb{Z}^2)$,

$$(8) \quad c \|q\|_2 \leq \left\| \sum_{\alpha \in \mathbb{Z}^2} q(\alpha) \phi(\cdot - \alpha) \right\|_2 \leq C \|q\|_2.$$

Stable functions ϕ and ϕ^d are called a *dual pair* when they satisfy

$$\langle \phi, \phi^d(\cdot - \alpha) \rangle = \begin{cases} 1, & \alpha = 0; \\ 0, & \alpha \in \mathbb{Z}^2 \setminus \{(0, 0)\}. \end{cases}$$

We will denote the refinement mask of ϕ^d by a^d .

For a given compactly supported refinable stable function $\phi \in \mathcal{L}_2(\mathbb{R}^2)$, define $S(\phi) \subset \mathcal{L}_2(\mathbb{R}^2)$ to be the smallest closed shift-invariant subspace generated by ϕ and define

$$S^k(\phi) := \{u(2^k \cdot) : u \in S(\phi)\}, \quad k \in \mathbb{Z}.$$

Then the sequence $S^k(\phi)$, $k \in \mathbb{Z}$, forms a multiresolution analysis of $\mathcal{L}_2(\mathbb{R}^2)$. Here we recall that a sequence $S^k(\phi)$ forms a *multiresolution analysis* when the following conditions are satisfied: (i) $S^k(\phi) \subset S^{k+1}(\phi)$; (ii) $\cup_{k \in \mathbb{Z}} S^k(\phi) = \mathcal{L}_2(\mathbb{R}^2)$ and $\cap_{k \in \mathbb{Z}} S^k(\phi) = \{0\}$; (iii) ϕ and its shifts form a Riesz basis of $S(\phi)$; see [5]. The sequence $S^k(\phi^d)$, $k \in \mathbb{Z}$, also forms a multiresolution analysis of $\mathcal{L}_2(\mathbb{R}^2)$.

The tensor product of univariate refinable functions and wavelets used in this paper will be derived from the following examples.

Example 1 (see [5, p. 277]). For 2×2 sensor arrays, using the rectangular rule for (2), we get L_2 in (6). Correspondingly, the refinement mask m is the piecewise linear spline, i.e.,

$$m(-1) = \frac{1}{4}, \quad m(0) = \frac{1}{2}, \quad m(1) = \frac{1}{4},$$

and $m(\alpha) = 0$ for all other α . The nonzero terms of the dual mask of m used in this paper are

$$m^d(-2) = -\frac{1}{8}, \quad m^d(-1) = \frac{1}{4}, \quad m^d(0) = \frac{3}{4}, \quad m^d(1) = \frac{1}{4}, \quad m^d(2) = -\frac{1}{8}.$$

In general, the tensor product bivariate filters for the dilation $2I$, where I is the identity matrix, are generated as follows. Let ϕ and ϕ^d be a dual pair of the univariate refinable functions with refinement masks m and m^d , respectively. Then, the biorthonormal wavelets ψ and ψ^d are defined by

$$\psi := 2 \sum_{\alpha \in \mathbb{Z}} r(\alpha) \phi(2 \cdot -\alpha) \quad \text{and} \quad \psi^d := 2 \sum_{\alpha \in \mathbb{Z}} r^d(\alpha) \phi^d(2 \cdot -\alpha),$$

where

$$r(-1) = \frac{1}{8}, \quad r(0) = \frac{1}{4}, \quad r(1) = -\frac{3}{4}, \quad r(2) = \frac{1}{4}, \quad r(3) = \frac{1}{8}$$

and

$$r^d(0) = \frac{1}{4}, \quad r^d(1) = -\frac{1}{2}, \quad r^d(2) = \frac{1}{4}$$

are the wavelet masks; see, for example, [5] for details. The tensor product dual pair of the refinement symbols are given by $\widehat{a}(\omega) = \widehat{m}(\omega_1)\widehat{m}(\omega_2)$, $\widehat{a}^d(\omega) = \widehat{m}^d(\omega_1)\widehat{m}^d(\omega_2)$, and the corresponding wavelet symbols are $\widehat{b}_{(0,1)}(\omega) = \widehat{m}(\omega_1)\widehat{r}(\omega_2)$, $\widehat{b}_{(0,1)}^d(\omega) = \widehat{m}^d(\omega_1)\widehat{r}^d(\omega_2)$, $\widehat{b}_{(1,0)}(\omega) = \widehat{r}(\omega_1)\widehat{m}(\omega_2)$, $\widehat{b}_{(1,0)}^d(\omega) = \widehat{r}^d(\omega_1)\widehat{m}^d(\omega_2)$, $\widehat{b}_{(1,1)}(\omega) = \widehat{r}(\omega_1)\widehat{r}(\omega_2)$, $\widehat{b}_{(1,1)}^d(\omega) = \widehat{r}^d(\omega_1)\widehat{r}^d(\omega_2)$, where $\omega = (\omega_1, \omega_2)$.

Although we give here only the details of refinable functions and their corresponding wavelets with dilation $2I$, the whole theory can be carried over to the general isotropic integer dilation matrices. The details can be found in [10] and the references therein. In the next example, we give the refinable and wavelet masks with dilation $4I$ that are used to generate the matrices for 4×4 sensor arrays.

Example 2. For 4×4 sensor arrays, using the rectangular rule for (2), we get L_4 in (6). The corresponding mask is

$$m(\alpha) = \frac{1}{8}, \frac{1}{4}, \frac{1}{4}, \frac{1}{4}, \frac{1}{8}, \quad \alpha = -2, \dots, 2,$$

with $m(\alpha) = 0$ for all other α . It is the mask of a stable refinable function ϕ with dilation 4 (see, e.g., [16] for a proof). The nonzero terms of a dual mask of m are

$$m^d(\alpha) = -\frac{1}{16}, \frac{1}{8}, \frac{5}{16}, \frac{1}{4}, \frac{5}{16}, \frac{1}{8}, -\frac{1}{16}, \quad \alpha = -3, \dots, 3.$$

The nonzero terms of the corresponding wavelet masks (see [20]) are

$$r_1(\alpha) = -\frac{1}{8}, -\frac{1}{4}, 0, \frac{1}{4}, \frac{1}{8}, \quad \alpha = -2, \dots, 2,$$

$$r_2(\alpha) = -\frac{1}{16}, -\frac{1}{8}, \frac{5}{16}, -\frac{1}{4}, \frac{5}{16}, -\frac{1}{8}, -\frac{1}{16}, \quad \alpha = -2, \dots, 4,$$

$$r_3(\alpha) = \frac{1}{16}, \frac{1}{8}, -\frac{7}{16}, 0, \frac{7}{16}, -\frac{1}{8}, -\frac{1}{16}, \quad \alpha = -2, \dots, 4.$$

The dual wavelet masks are

$$r_1^d(\alpha) = (-1)^{1-\alpha} r_3(1-\alpha), \quad r_2^d(\alpha) = (-1)^{1-\alpha} m(1-\alpha), \quad r_3^d(\alpha) = (-1)^{1-\alpha} r_1(1-\alpha),$$

for appropriate α .

In the next two subsections, we will use the wavelet approach to design algorithms for recovering the high-resolution image from the low-resolution images of a true image. In section 3.1, we first consider the true image as a representation of a function in a certain subspace of $L_2(\mathbb{R}^2)$, and using wavelet means we recover this function from the given set of low-resolution images. In section 3.2, we translate the wavelet algorithms into matrix terminologies.

3.1. Function reconstruction. Since $S^k(\phi^d)$, $k \in \mathbb{Z}$, forms a multiresolution analysis of $L_2(\mathbb{R}^2)$, we can assume without loss of generality that the pixel values of the original image are the coefficients of a function f in $S^k(\phi^d)$ for some k . The pixel values of the low-resolution images can be considered as the coefficients of a function g in $S^{k-1}(\phi^d)$ and its $1/2^k$ translates, i.e., g is represented by $\phi^d(2^{k-1}(\cdot - \alpha/2^k))$ with $\alpha \in \mathbb{Z}^2$. The low-resolution images keep most of the low-frequency information of f and the high-frequency information in f is folded by the lowpass filter a . Hence, to recover f , the high-frequency information of f hidden in the low-resolution images will be unfolded and combined with the low-frequency information to restore f . We will unfold the high-frequency content iteratively using the wavelet decomposition and reconstruction algorithms.

For 2×2 sensor arrays, the multiresolution analysis $S^k(\phi^d)$ used is from a refinable function with dilation matrix $2I$. In general, $K \times K$ sensor arrays can be analyzed by the multiresolution analysis generated by a refinable function with dilation matrix $K \cdot I$. For simplicity, we give the analysis for the case that the dilation matrix is $2I$ and $k = 1$. A similar analysis can be carried out for more general cases.

Let $f \in S^1(\phi^d)$. Then,

$$(9) \quad f = \sum_{\alpha \in \mathbb{Z}^2} \langle f, 2\phi(2 \cdot -\alpha) \rangle 2\phi^d(2 \cdot -\alpha) := 2 \sum_{\alpha \in \mathbb{Z}^2} v(\alpha) \phi^d(2 \cdot -\alpha).$$

The numbers $v(\alpha)$, $\alpha \in \mathbb{Z}^2$, are the pixel values of the high-resolution image we are seeking, and they form the discrete representation of f under the basis $2\phi^d(2 \cdot -\alpha)$, $\alpha \in \mathbb{Z}^2$. The given data set $(a * v)(\alpha)$ is the observed high-resolution image. By using the refinability of ϕ^d , one finds that $a * v$ is the coefficient sequence of the function g represented by $\phi^d(\cdot - \alpha/2)$, $\alpha \in \mathbb{Z}^2$, in $S^1(\phi^d)$. We call this g the *observed function* and it is given by

$$(10) \quad g := \sum_{\alpha \in \mathbb{Z}^2} (a * v)(\alpha) \phi^d(\cdot - \alpha/2).$$

The observed function can be obtained precisely once $a * v$ is given.

When only $a * v$ is given, to recover f , one first finds v from $a * v$ and then derives f using the basis $2\phi^d(2 \cdot -\alpha)$, $\alpha \in \mathbb{Z}^2$, as in (9). Here we provide an iterative algorithm to recover v . At step $(n+1)$ of the algorithm, it improves the high-frequency components of f by updating the high-frequency components of the previous step. The algorithm is presented in the Fourier domain, where the problem becomes the following: for a given $\widehat{a * v} = \widehat{av}$, one needs to find \widehat{v} in order to restore f .

Denote $\mathbb{Z}_2^2 = \{(0,0), (0,1), (1,0), (1,1)\}$. Our algorithm will make use of the following fact from the biorthogonal wavelet theory: for a given tensor product bivariate refinement mask a corresponding to a stable refinable function ϕ , one can find a tensor product dual mask a^d and the corresponding wavelet masks b_ν and b_ν^d , $\nu \in \mathbb{Z}_2^2 \setminus \{(0,0)\}$, such that the symbols of the refinement masks and wavelet masks satisfy the following equation [5]:

$$(11) \quad \overline{\widehat{a}^d \widehat{a}} + \sum_{\nu \in \mathbb{Z}_2^2 \setminus \{(0,0)\}} \widehat{b}_\nu^d \widehat{b}_\nu = 1.$$

We note that when the refinable function ϕ of the convolution kernel a and its shifts form an orthonormal system (e.g., in the Haar case), then (11) holds if we choose $\widehat{a}^d = \widehat{a}$ and $\widehat{b}_\nu^d = \widehat{b}_\nu$. This leads to orthonormal wavelets. When ϕ and its shifts form only a Riesz system, one has to use biorthogonal wavelets.

By (11), we have $\widehat{v} = \widehat{\overline{a}^d a * v} + (\sum_{\nu \in \mathbb{Z}_2^2 \setminus \{(0,0)\}} \widehat{b}_\nu^d \widehat{b}_\nu) \widehat{v}$. Hence we have the following algorithm.

ALGORITHM 1.

- (i) Choose $\widehat{v}_0 \in \mathcal{L}_2[-\pi, \pi]^2$;
- (ii) Iterate until convergence:

$$(12) \quad \widehat{v}_{n+1} = \widehat{\overline{a}^d a * v} + \left(\sum_{\nu \in \mathbb{Z}_2^2 \setminus \{(0,0)\}} \widehat{b}_\nu^d \widehat{b}_\nu \right) \widehat{v}_n.$$

We remark that the first term $\widehat{\overline{a}^d a * v} = \widehat{\overline{a}^d a} \widehat{v}$ in the right-hand side of (12) represents the approximation of the low-frequency components of f , whereas the second term improves the high-frequency approximation.

Given \widehat{v}_n , f_n is defined via its Fourier transform as

$$(13) \quad \widehat{f}_n(\cdot) := \widehat{v}_n(\cdot/2) \widehat{\phi}^d(\cdot/2) \in S^1(\phi^d).$$

Strictly speaking, \widehat{f}_n and $\widehat{\phi}^d$ are the Fourier transform of, respectively, f and ϕ while \widehat{v}_n is the symbol of the sequence v_n . But here to simplify the notation, we will use the same “hat” notation to denote both. We now show that the functions f_n converge to the function f in (9).

PROPOSITION 3.1. *Let ϕ and ϕ^d be a pair of dual refinable functions with refinement masks a and a^d and let b_ν and b_ν^d , $\nu \in \mathbb{Z}_2^2 \setminus \{(0,0)\}$, be the wavelet masks of the corresponding biorthogonal wavelets. Suppose that $0 \leq \overline{\widehat{a}^d \widehat{a}} \leq 1$ and its zero set has measure zero. Then, the sequence \widehat{v}_n defined in (12) converges to \widehat{v} in the \mathcal{L}_2 -norm for any arbitrary $\widehat{v}_0 \in \mathcal{L}_2[-\pi, \pi]^2$. In particular, f_n in (13) converges to f in (9) in the \mathcal{L}_2 -norm.*

Proof. For an arbitrary $\widehat{v}_0 \in \mathcal{L}_2[-\pi, \pi]^2$, applying (12), we have

$$\widehat{v} - \widehat{v}_n = \left(\sum_{\nu \in \mathbb{Z}_2^2 \setminus \{(0,0)\}} \widehat{b}_\nu^d \widehat{b}_\nu \right)^n (\widehat{v} - \widehat{v}_0).$$

It follows from $0 \leq \overline{\widehat{a}^d \widehat{a}} \leq 1$ and (11) that

$$\left| \sum_{\nu \in \mathbb{Z}_2^2 \setminus \{(0,0)\}} \widehat{b}_\nu^d \widehat{b}_\nu \right| \leq 1.$$

Since $\widehat{a}^d \widehat{a} \geq 0$ and its zero set has measure zero, the inequality

$$\left| \sum_{\nu \in \mathbb{Z}_2^2 \setminus \{(0,0)\}} \widehat{b}_\nu^d \widehat{b}_\nu \right| < 1$$

holds almost everywhere. Hence,

$$\left(\sum_{\nu \in \mathbb{Z}_2^2 \setminus \{(0,0)\}} \widehat{b}_\nu^d \widehat{b}_\nu \right)^n (\widehat{v} - \widehat{v}_0) \rightarrow 0, \quad \text{as } n \rightarrow \infty \text{ a.e.}$$

By the dominated convergence theorem (see, e.g., [19]), \widehat{v}_n converges to \widehat{v} in the \mathcal{L}_2 -norm.

Since $\phi^d(\cdot - \alpha)$ is a Riesz basis of $S^0(\phi^d)$, from (8), $2\phi^d(2 \cdot - \alpha)$ is a Riesz basis of $S^1(\phi^d)$. Hence by (8) again,

$$\begin{aligned} \|f_n - f\|_2 &= \left\| \sum_{\alpha \in \mathbb{Z}^2} (v_n(\alpha) - v(\alpha)) 2\phi(2 \cdot - \alpha) \right\|_2 \\ &\leq C \|v_n - v\|_2 = \frac{C}{2\pi} \|\widehat{v}_n - \widehat{v}\|_2 \longrightarrow 0. \quad \square \end{aligned}$$

Remark 1. The symbols of the refinement masks and the corresponding dual masks used in this paper are tensor products of univariate ones that satisfy the assumptions of this proposition.

Remark 2. The above convergence result is also applicable to the super-resolution case. Assume for simplicity that $a * v$ is downsampled to four subsamples $(a * v)(\nu - 2\alpha)$, $\nu \in \mathbb{Z}_2^2$. For the super-resolution case, one only has some of the subsamples, $(a * v)(\nu - 2\alpha)$, $\nu \in A \subset \mathbb{Z}_2^2$. In this case, one first applies an interpolatory scheme (e.g., [10]) to obtain the full set of the sample w approximately. Let the ℓ_2 solution of the equation $a * z = w$ be u . Then, $(a * u)(\nu - 2\alpha) = (a * v)(\nu - 2\alpha)$ for $\nu \in A$. Applying Algorithm 1 to $a * u$, the above proposition asserts that it converges to u .

When there is noise in the given data $a * v$, one may subtract some high-frequency components from \widehat{v}_n at each iteration to reduce the noise, since noise is in the high-frequency components. Then we get the following modified algorithm.

ALGORITHM 2.

- (i) Choose $\widehat{v}_0 \in \mathcal{L}_2[-\pi, \pi]^2$;
- (ii) Iterate until convergence:

$$(14) \quad \widehat{v}_{n+1} = \widehat{a}^d \widehat{a} * \widehat{v} + (1 - \beta) \left(\sum_{\nu \in \mathbb{Z}_2^2 \setminus \{(0,0)\}} \widehat{b}_\nu^d \widehat{b}_\nu \right) \widehat{v}_n, \quad 0 < \beta < 1.$$

In this denoising procedure, the high-frequency components are penalized uniformly by the factor $(1 - \beta)$. This smoothes the original signals while denoising.

To remedy this, we now introduce a wavelet thresholding denoising method. It is based on the observation that $\widehat{b}_\nu \widehat{v}_n = \widehat{b_\nu * v_n}$, $\nu \in \mathbb{Z}_2^2 \setminus \{(0,0)\}$, are the exact wavelet coefficients of the wavelet decomposition (without downsampling) of the function f_n , the n th approximation of f . A further decomposition of $b_\nu * v_n$, by using the lowpass filter a and the highpass filters b_ν several times, will give the wavelet coefficients of

the decomposition of f_n by the translation-invariant wavelet packets defined by the biorthogonal filters a , a^d and b_ν , b_ν^d (see, e.g., [17] and [25]). More precisely, by using (11) we have

$$\widehat{b}_\nu \widehat{v}_n = \left(\overline{\widehat{a}^d} \right)^J (\widehat{a})^J \widehat{b}_\nu \widehat{v}_n + \sum_{j=0}^{J-1} \left(\overline{\widehat{a}^d} \right)^j \sum_{\gamma \in \mathbb{Z}_2^2 \setminus \{(0,0)\}} \widehat{b}_\gamma^d \widehat{b}_\gamma (\widehat{a})^j \widehat{b}_\nu \widehat{v}_n,$$

where J is the number of levels used to decompose $\widehat{b}_\nu \widehat{v}_n$. For each j and $\gamma \in \mathbb{Z}_2^2 \setminus \{(0,0)\}$, $\widehat{b}_\gamma (\widehat{a})^j \widehat{b}_\nu \widehat{v}_n$ are the coefficients of the wavelet packet (see, e.g., [25]) down to the j th level. A wavelet thresholding denoising procedure is then applied to $\widehat{b}_\gamma (\widehat{a})^j \widehat{b}_\nu \widehat{v}_n$, the coefficients of the wavelet packet decomposition of f_n , before $b_\nu * v_n$ is reconstructed back by the dual masks. This denoises the function f_n . Our method keeps the features of the original signal. Moreover, since we do not downsample (by a factor of 2) in the decomposition procedure, we are essentially using a translation-invariant wavelet packet system [17], which is a highly redundant system. As was pointed out in [4] and [17], a redundant system is desirable in denoising, since it reduces the Gibbs oscillations.

Another potential problem with Algorithm 2 is that at each iteration, \widehat{v}_{n+1} inherits the noise from the observed data $\widehat{a * v}$ present in the first term on the right-hand side of (14). If the algorithm converges at the n_0 th step, then \widehat{v}_{n_0} still carries the noise from $\widehat{a * v}$. One can eliminate part of these noise by passing the final iterate \widehat{v}_{n_0} through the wavelet thresholding scheme we mentioned above (see step (iii) below). We summarize our thresholding method in the following algorithm.

ALGORITHM 3.

- (i) Choose $\widehat{v}_0 \in \mathcal{L}_2[-\pi, \pi]^2$;
- (ii) Iterate until convergence:

$$\widehat{v}_{n+1} = \overline{\widehat{a}^d} \widehat{a * v} + \sum_{\nu \in \mathbb{Z}_2^2 \setminus \{(0,0)\}} \widehat{b}_\nu^d \mathcal{T}(\widehat{b}_\nu \widehat{v}_n),$$

where

$$\mathcal{T}(\widehat{b}_\nu \widehat{v}_n) = \left(\overline{\widehat{a}^d} \right)^J (\widehat{a})^J \widehat{b}_\nu \widehat{v}_n + \sum_{j=0}^{J-1} \left(\overline{\widehat{a}^d} \right)^j \sum_{\gamma \in \mathbb{Z}_2^2 \setminus \{(0,0)\}} \widehat{b}_\gamma^d \mathcal{D}(\widehat{b}_\gamma (\widehat{a})^j \widehat{b}_\nu \widehat{v}_n),$$

and \mathcal{D} is a thresholding operator (see, for instance, (19) below).

- (iii) Let \widehat{v}_{n_0} be the final iterate from step (ii). The final solution of our algorithm is

$$\widehat{v}_c = \left(\overline{\widehat{a}^d} \right)^J (\widehat{a})^J \widehat{v}_{n_0} + \sum_{j=0}^{J-1} \left(\overline{\widehat{a}^d} \right)^j \sum_{\gamma \in \mathbb{Z}_2^2 \setminus \{(0,0)\}} \widehat{b}_\gamma^d \mathcal{D}(\widehat{b}_\gamma (\widehat{a})^j \widehat{v}_{n_0}),$$

where \mathcal{D} is the same thresholding operator used in step (ii).

In both the regularization method (Algorithm 2) and the thresholding method (Algorithm 3), the n th approximation f_n is denoised before it is added to the iterate to improve the approximation. The major difference between Algorithms 2 and 3 is that step (ii) in Algorithm 2 is replaced by step (ii) of Algorithm 3, where the thresholding denoising procedure is built in.

3.2. Image reconstruction. Let us now translate the results above from wavelet notations into matrix terminologies. Denote by L , L^d , H_ν^d , and H_ν the matrices generated by the symbols of the refinement and wavelet masks \hat{a} , \hat{a}^d , \hat{b}_ν , and \hat{b}_ν^d , respectively. For the periodic boundary conditions, the matrix L is already given in (5) and the matrices L^d , H_ν^d , and H_ν will be given in detail in section 4. Using these matrices, (11) can be written as

$$(15) \quad L^d L + \sum_{\nu \in \mathbb{Z}_2^2 \setminus \{(0,0)\}} H_\nu^d H_\nu = I.$$

Also, (12) can be written as

$$(16) \quad \mathbf{f}_{n+1} = L^d \mathbf{g} + \left(\sum_{\nu \in \mathbb{Z}_2^2 \setminus \{(0,0)\}} H_\nu^d H_\nu \right) \mathbf{f}_n,$$

where \mathbf{g} ($\sim a * v$) is the observed high-resolution image given in (4) and \mathbf{f}_n are the approximations of \mathbf{f} at the n th iteration.

Rewriting (16) as

$$\mathbf{f}_{n+1} - \left(\sum_{\nu \in \mathbb{Z}_2^2 \setminus \{(0,0)\}} H_\nu^d H_\nu \right) \mathbf{f}_n = L^d \mathbf{g},$$

one sees that it is a stationary iteration for solving the matrix equation

$$\left[I - \left(\sum_{\nu \in \mathbb{Z}_2^2 \setminus \{(0,0)\}} H_\nu^d H_\nu \right) \right] \mathbf{f} = L^d \mathbf{g}.$$

Therefore by (15), we get the matrix form of Algorithm 1.

ALGORITHM 1 (in matrix form).

$$(17) \quad L^d L \mathbf{f} = L^d \mathbf{g}.$$

We note that there is no need to iterate on (16) to get \mathbf{f} .

In a similar vein, one can show that Algorithm 2 is actually a stationary iteration for the matrix equation

$$\left(L^d L + \beta \sum_{\nu \in \mathbb{Z}_2^2 \setminus \{(0,0)\}} H_\nu^d H_\nu \right) \mathbf{f} = L^d \mathbf{g}.$$

Here, β is a regularization parameter. By (15), this reduces to the following algorithm.

ALGORITHM 2 (in matrix form).

$$(18) \quad \left(L^d L + \frac{\beta}{1-\beta} I \right) \mathbf{f} = \frac{1}{1-\beta} L^d \mathbf{g}.$$

Again, there is no need to iterate on (14) to get \mathbf{f} . For periodic boundary conditions, both the matrices L and L^d in (18) are BCCB matrices of size $M_1 M_2 \times M_1 M_2$ and hence (18) can be solved efficiently by using three 2D FFTs in $O(M_1 M_2 \log(M_1 M_2))$

operations; see [9, section 5.2.2]. For symmetric boundary conditions, both matrices L and L^d are block Toeplitz-plus-Hankel matrices with Toeplitz-plus-Hankel blocks. Thus (18) can be solved by using three 2D FCTs in $O(M_1 M_2 \log(M_1 M_2))$ operations (see [18]). It is interesting to note that (18) is similar to the Tikhonov least-squares method (7), except that instead of L^* , we use L^d .

In (16), it is easy to further decompose $H_\nu \mathbf{f}_n$, $\nu \in \mathbb{Z}_2^2 \setminus \{(0,0)\}$, by applying the matrices L and H_γ , $\gamma \in \mathbb{Z}_2^2 \setminus \{(0,0)\}$, to obtain the wavelet packet decomposition of \mathbf{f}_n . Then we can apply the threshold denoising method we have discussed in section 3.1. To present the matrix form of Algorithm 3, we define Donoho's thresholding operator [7]. For a given λ , let

$$(19) \quad \mathcal{D}_\lambda((x_1, \dots, x_l, \dots)^T) = (t_\lambda(x_1), \dots, t_\lambda(x_l), \dots)^T,$$

where the thresholding function t_λ is either (i) $t_\lambda(x) = x \chi_{|x| > \lambda}$, referred to as the *hard threshold*, or (ii) $t_\lambda(x) = \text{sgn}(x) \max(|x| - \lambda, 0)$, the *soft threshold*.

ALGORITHM 3 (in matrix form).

- (i) Choose an initial approximation \mathbf{f}_0 (e.g., $\mathbf{f}_0 = L^d \mathbf{g}$);
- (ii) Iterate until convergence:

$$\mathbf{f}_{n+1} = L^d \mathbf{g} + \sum_{\nu \in \mathbb{Z}_2^2 \setminus \{(0,0)\}} H_\nu^d \mathcal{T}(H_\nu \mathbf{f}_n).$$

Here

$$(20) \quad \mathcal{T}(H_\nu \mathbf{f}_n) = (L^d)^J (L)^J (H_\nu \mathbf{f}_n) + \sum_{j=0}^{J-1} (L^d)^j \sum_{\gamma \in \mathbb{Z}_2^2 \setminus \{(0,0)\}} H_\gamma^d \mathcal{D}_{\lambda_{n,\nu}}(H_\gamma (L)^j H_\nu \mathbf{f}_n)$$

with $\mathcal{D}_{\lambda_{n,\nu}}$ given in (19) and $\lambda_{n,\nu} = \sigma_{n,\nu} \sqrt{2 \log(M_1 M_2)}$, where $\sigma_{n,\nu}$ is the variance of $H_\nu \mathbf{f}_n$ estimated numerically by the method provided in [7].

- (iii) Let \mathbf{f}_{n_0} be the final iterate from step (ii). The final solution of our algorithm is

$$\mathbf{f}_c = (L^d)^J (L)^J \mathbf{f}_{n_0} + \sum_{j=0}^{J-1} (L^d)^j \sum_{\gamma \in \mathbb{Z}_2^2 \setminus \{(0,0)\}} H_\gamma^d \mathcal{D}_{\lambda_{n_0}}(H_\gamma (L)^j \mathbf{f}_{n_0}),$$

where $\mathcal{D}_{\lambda_{n_0}}$ is the thresholding operator used in step (ii).

According to [7], the choice of $\lambda_{n,\nu}$ in step (ii) is a good thresholding level for orthonormal wavelets as well as biorthonormal wavelets.

The computational complexity of Algorithm 3 depends on the number of iterations required for convergence. In each iteration, we essentially go through a J -level wavelet decomposition and reconstruction procedure once; therefore it needs $O(M_1 M_2)$ operations. As for the value of J , the larger it is, the finer the wavelet packet decomposition of \mathbf{f}_n will be before it is denoised. This leads to a better denoising scheme. However, a larger J will cost slightly more computational time. From our numerical tests, we find that it is already good enough to choose J to be either 1 or 2. The variance $\sigma_{n,\nu}$ is estimated by the method given in [7] which uses the median of the absolute value of the entries in the vector $H_\nu \mathbf{f}_n$. Hence the cost of computing $\sigma_{n,\nu}$ is $O(M_1 M_2 \log(M_1 M_2))$; see for instance [21]. Finally, the cost of step (iii) is less than one additional iteration of step (ii). One nice feature of Algorithm 3 is that it is parameter-free—we do

not have to choose the regularization parameter β as in the Tikhonov method (7) or Algorithm 2.

For the super-resolution case, where only some of the subsamples $(a * v)(\nu - 2\alpha)$, $\nu \in A \subset \mathbb{Z}_2^2$, are available, we can first apply an interpolatory scheme (e.g., interpolatory subdivision scheme in [6] and [10]) to obtain the full set of the sample \mathbf{w} approximately. Then, with \mathbf{w} as the observed image, we find an approximation solution \mathbf{u} from either Algorithm 2 or Algorithm 3. To tune up the result, we can compute $L\mathbf{u}$ to obtain $(a * u)(\nu - 2\alpha)$, $\nu \in \mathbb{Z}_2$, and replace the component $(a * u)(\nu - 2\alpha)$, $\nu \in A$, by the sample data, i.e., $(a * v)(\nu - 2\alpha)$, $\nu \in A$. With this new observed high-resolution image, we again use either Algorithm 2 or Algorithm 3 to get the final high-resolution image \mathbf{f} .

4. Numerical experiments. In this section, we implement the wavelet algorithms developed in the last section to one-dimensional (1D) and 2D examples and compare them with the Tikhonov least-squares method. We evaluate the methods using the relative error (RE) and the peak signal-to-noise ratio (PSNR), which compare the reconstructed signal (image) \mathbf{f}_c with the original signal (image) \mathbf{f} . They are defined by

$$\text{RE} = \frac{\|\mathbf{f} - \mathbf{f}_c\|_2}{\|\mathbf{f}\|_2}$$

and

$$\text{PSNR} = 10 \log_{10} \frac{\|\mathbf{f}\|_2^2}{\|\mathbf{f} - \mathbf{f}_c\|_2^2},$$

for 1D signals, and

$$\text{PSNR} = 10 \log_{10} \frac{255^2 NM}{\|\mathbf{f} - \mathbf{f}_c\|_2^2},$$

for 2D images, respectively, where the size of the signals (images) is $N \times M$.

In our tests, $N = 1$ for 1D signals while $N = M$ for 2D images. For the Tikhonov method (7), we will use the identity matrix I as the regularization operator R . For both (7) and Algorithm 2, the optimal regularization parameters β^* are chosen by trial and error so that they give the best PSNR values for the resulting equations. For Algorithm 3, we use the hard thresholding for \mathcal{D}_λ in (19) and $J = 1$ in (20), and we stop the iteration as soon as the values of PSNR peak. The number of iterations for Algorithm 3 is denoted as Ite.

4.1. Numerical simulation for 1D signals. To emphasize that our algorithms work for general deblurring problems, we first apply our algorithms to two 1D blurred and noisy signals. The blurring is done by the filter given in Example 2. The matrices L^d , L , H_p^d , and H_p , $p = 1, 2, 3$, are generated by the corresponding univariate symbols of the refinement and wavelet masks $\widehat{m^d}$, \widehat{m} , $\widehat{r_p^d}$, and $\widehat{r_p}$, respectively (with either periodic or symmetric boundary conditions). For example, the matrix L for the periodic boundary condition is given by the matrix L_4 in (6) (cf. section 4.2.1 for how to generate the other matrices).

The Tikhonov method (7) and Algorithm 2 reduce to solving the linear systems

$$(L^* L + \beta I)\mathbf{f} = L^* \mathbf{g} \quad \text{and} \quad \left(L^d L + \frac{\beta}{1-\beta} I \right) \mathbf{f} = \frac{1}{1-\beta} L^d \mathbf{g},$$

respectively. For Algorithm 3, steps (ii) and (iii) become

$$\begin{aligned}\mathbf{f}_{n+1} &= L^d \mathbf{g} + \sum_{p=1}^3 H_p^d \left(L^d L H_p \mathbf{f}_n + \sum_{q=1}^3 H_q^d \mathcal{D}_{\lambda_{n,p}}(H_q H_p \mathbf{f}_n) \right), \\ \mathbf{f}_c &= L^d L \mathbf{f}_{n_0} + \sum_{p=1}^3 H_p^d \mathcal{D}_{\lambda_{n,p}}(H_p \mathbf{f}_{n_0}).\end{aligned}$$

The 1D signals in our test are taken from the WaveLab toolbox at <http://www-stat.stanford.edu/~wavelab/> developed by Donoho's research group. Figure 2(a) shows the first original signal \mathbf{f} . Figure 2(b) depicts the blurred and contaminated signal with white noise at signal-to-noise ratio (SNR) = 25. The results of deblurring by (7), Algorithm 2, and Algorithm 3 with periodic boundary conditions are shown in Figures 2(c)–(e), respectively.

It is clear from Figure 2 that Algorithm 3 outperforms the other two methods. When the symmetric boundary condition is used, the numerical results for each algorithm are almost the same as that of the corresponding algorithms with the periodic boundary condition. Hence, we omit the figures here. The similarity of the performance for the two different boundary conditions is due to the fact that the extensions of the signal by both boundary conditions are very close. (Note that the original signal has almost the same values at the two end points.)

In the second example (Figure 3), the different boundary conditions lead to different extensions of the signal. It is therefore not surprising to see in Figure 3 that the symmetric boundary condition gives better PSNR values and visual quality than those of the periodic one. We omit the figures generated by Algorithm 2 for this example. The numerical results from both tests show clearly that Algorithm 3 (the thresholding method) outperforms the regularization methods (the least-squares method and Algorithm 2). To see exactly how Algorithm 3 performs, we show in Figure 4(a)–(e) the intermediate results in each of the five iterations of step (ii) in Algorithm 3. Let us look at the values of these five iterations at the point 0.4. They are 12.63, 13.20, 13.53, 13.80, and 13.99, respectively. The value of the original signal (see Figure 3(a)) is 15.17 at the point 0.4. Thus there are some improvements in each iteration. Figure 4(f) is the result after step (iii) of Algorithm 3.

4.2. High-resolution image reconstruction. This section illustrates the effectiveness of the high-resolution image reconstruction algorithm derived from the wavelet analysis. We use the “boat” image of size 260×260 and the “Lena” image of size 512×512 as the original images in our numerical tests. To simulate the real world situations, the pixel values of the low-resolution images near the boundary are obtained from the discrete equation of (2) by using the actual pixel values of the true images instead of imposing any boundary conditions on these pixels.

4.2.1. 2×2 sensor array. For 2×2 sensor arrays, (2) is equivalent to blurring the true image with a 2D lowpass filter a which is the tensor product of the lowpass filter given in Example 1. Gaussian white noise is added to the resulting blurred image, and it is then chopped to size 256×256 for the “boat” image and size 508×508 for the “Lena” image to form our observed high-resolution image \mathbf{g} . We note that the pixels of \mathbf{g} are already the pixels of the low-resolution images. Therefore the four 128×128 low-resolution frames for the “boat” image and the four 254×254 low-resolution

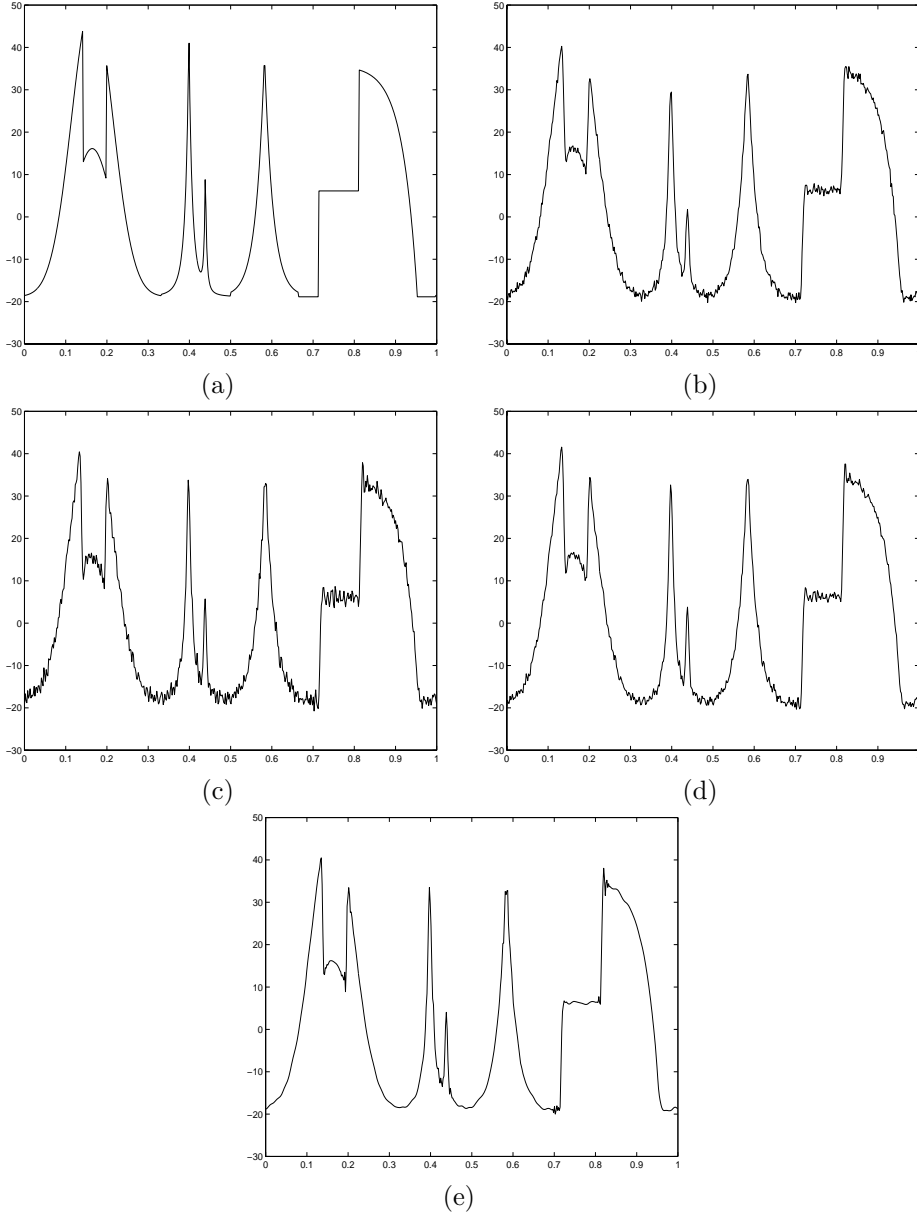


FIG. 2. (a) Original signal; (b) Observed signal, blurred by the filter a in Example 2 and contaminated by white noise at SNR = 25; (c) Reconstructed signal from the least-squares method with the identity regularization ($PSNR = 43.19dB$, $RE = 0.0987$, $\beta^* = 0.0402$); (d) Reconstructed signal from Algorithm 2 ($PSNR = 44.44dB$, $RE = 0.0855$, $\beta^* = 0.2205$); (e) Reconstructed signal from Algorithm 3 after 12 iterations ($PSNR = 45.75dB$, $RE = 0.0735$).

frames for the ‘‘Lena’’ image can be obtained by downsampling \mathbf{g} by a factor of 2 in both the horizontal and the vertical directions.

The vector \mathbf{g} is then used in the Tikhonov method (7), Algorithm 2, and Algorithm 3 to recover the high-resolution image vector \mathbf{f} . We recall from section 2 that the matrix system relating \mathbf{g} and \mathbf{f} is not a square system; in order to recover \mathbf{f} , we

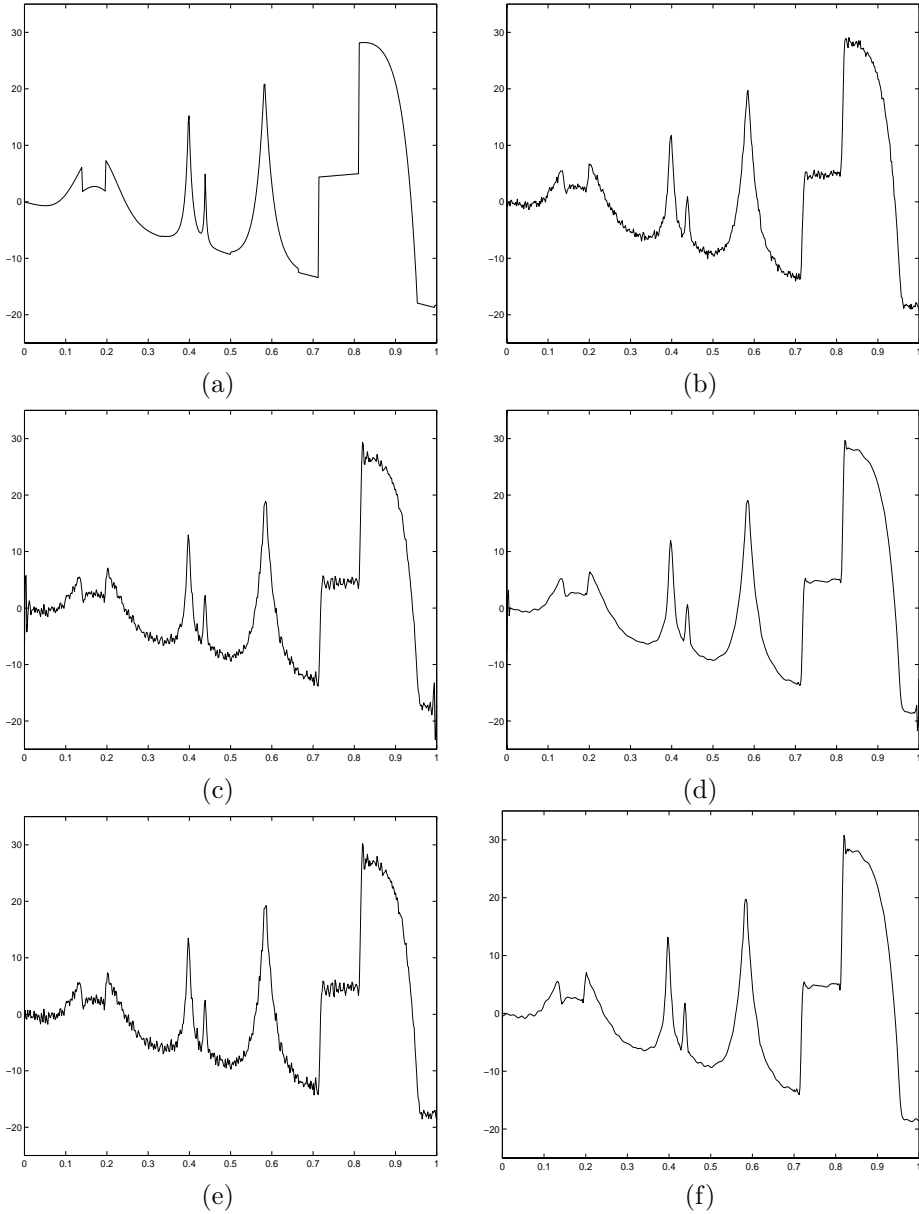


FIG. 3. (a) Original signal; (b) Observed signal, blurred by the filter a in Example 2 and contaminated by white noise at $SNR = 25$; (c) Reconstructed signal from the least-squares method with the identity regularization and periodic boundary conditions ($PSNR = 45.80dB$, $RE = 0.1183$, $\beta^* = 0.0619$); (d) Reconstructed signal from Algorithm 3 with periodic boundary condition and after 2 iterations ($PSNR = 48.90dB$, $RE = 0.0828$); (e) Reconstructed signal from the least-squares method with the identity regularization and symmetric boundary condition ($PSNR = 47.86dB$, $RE = 0.0933$, $\beta^* = 0.0421$); (f) Reconstructed signal from Algorithm 3 with symmetric boundary condition and after 5 iterations ($PSNR = 50.94dB$, $RE = 0.0654$).

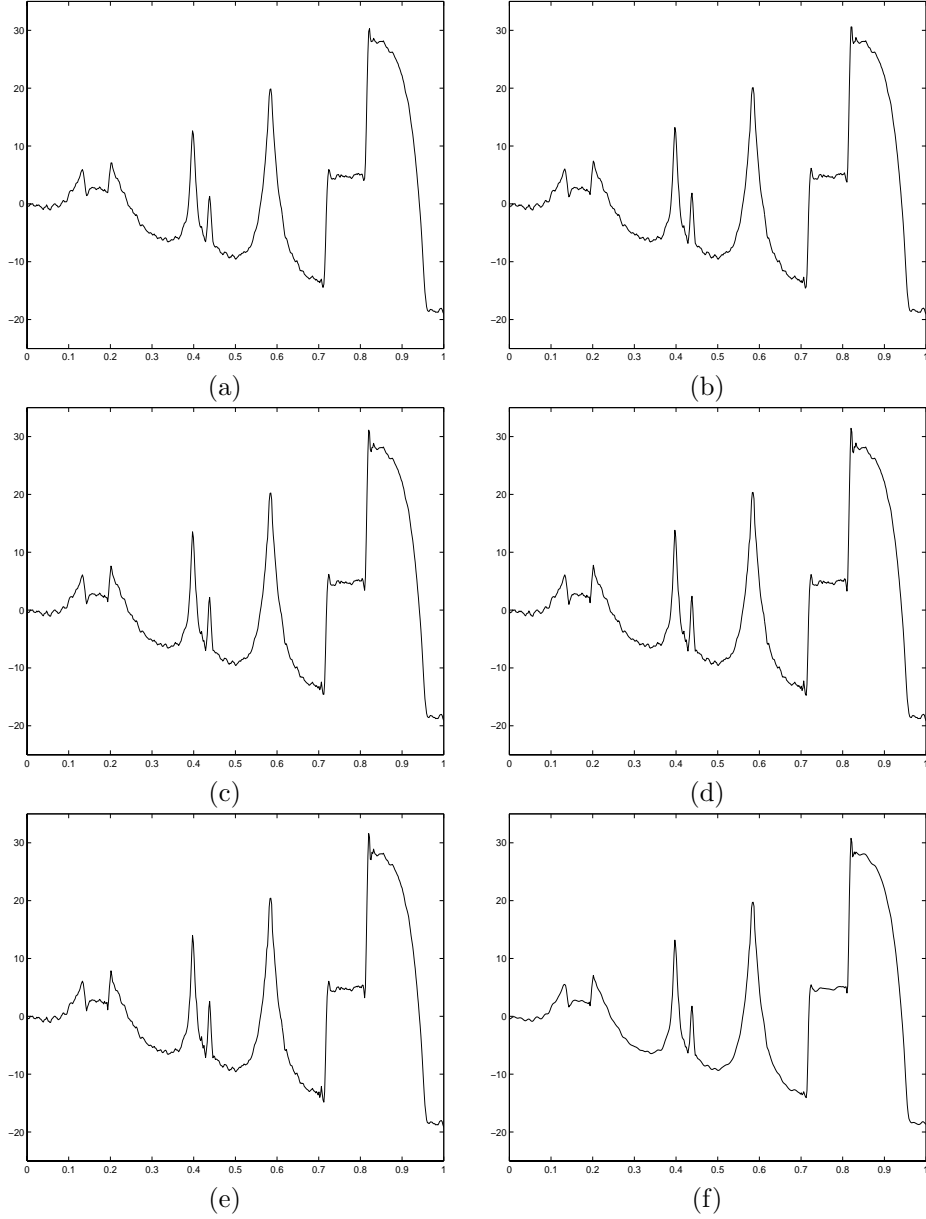


FIG. 4. (a)–(e) Reconstructed signals in the first five iterations of step (ii) of Algorithm 3, under symmetric boundary condition; (f) Reconstructed signal from step (iii) of Algorithm 3 from the signal shown in (e).

impose boundary assumptions on \mathbf{f} to make the matrix system a square system; see (4). We have tested both the periodic and symmetric boundary conditions for all three methods. For simplicity, we will only write out the matrices for the periodic case. The matrices for the symmetric boundary condition can be derived analogously; see [18, 2].

In what follows, all images are viewed as column vectors by reordering the entries

of the images in a rowwise order. For the periodic boundary conditions, both the Tikhonov method and Algorithm 2 are BCCB systems and hence can be solved efficiently by three 2D FFTs; see [9, section 5.2.2]. For symmetric boundary conditions, the systems can be solved by three 2D FCTs; see [18]. For Algorithm 3, we have $L = L_2 \otimes L_2$, $H_{(0,1)} = L_2 \otimes H_2$, $H_{(1,0)} = H_2 \otimes L_2$, $H_{(1,1)} = H_2 \otimes H_2$, $L^d = L_2^d \otimes L_2^d$, $H_{(0,1)}^d = L_2^d \otimes H_2^d$, $H_{(1,0)}^d = H_2^d \otimes L_2^d$, and $H_{(1,1)}^d = H_2^d \otimes H_2^d$. Here L_2 is given in (6) and

$$L_2^d \equiv \frac{1}{8} \begin{bmatrix} 6 & 2 & -1 & & & -1 & 2 \\ 2 & 6 & 2 & -1 & & & -1 \\ -1 & 2 & 6 & 2 & -1 & & \\ & -1 & 2 & 6 & 2 & -1 & \\ & & \ddots & \ddots & \ddots & \ddots & \ddots \\ & & & -1 & 2 & 6 & 2 & -1 \\ -1 & & & & -1 & 2 & 6 & 2 \\ 2 & -1 & & & & -1 & 2 & 6 \end{bmatrix},$$

$$H_2 \equiv \frac{1}{8} \begin{bmatrix} 2 & -6 & 2 & 1 & & & 1 \\ 1 & 2 & -6 & 2 & 1 & & \\ & 1 & 2 & -6 & 2 & 1 & \\ & & \ddots & \ddots & \ddots & \ddots & \ddots \\ & & & 1 & 2 & -6 & 2 & 1 \\ 1 & & & & 1 & 2 & -6 & 2 \\ 2 & 1 & & & & 1 & 2 & -6 \\ -6 & 2 & 1 & & & & 1 & 2 \end{bmatrix},$$

$$H_2^d \equiv \frac{1}{4} \begin{bmatrix} 1 & & 1 & -2 \\ -2 & 1 & & 1 \\ 1 & -2 & 1 & \\ \ddots & \ddots & \ddots & \\ & 1 & -2 & 1 \end{bmatrix}.$$

Tables 1 and 2 give the PSNR and RE values of the reconstructed images for different Gaussian noise levels, the optimal regularization parameter β^* for the Tikhonov method and Algorithm 2, and also the number of iterations required for step (ii) in Algorithm 3. For the periodic boundary condition, Algorithm 2 and Algorithm 3 are comparable and both are better than the Tikhonov method. For the symmetric boundary condition, Algorithm 3 performs better than both the Tikhonov method and Algorithm 2. In general, symmetric boundary conditions perform better than the periodic ones.

4.2.2. 4×4 sensor array. We have done similar numerical tests for the 4×4 sensor arrays. The bivariate filters are the tensor product of the filters in Example 2. The observed high-resolution image is generated by applying the bivariate lowpass filter on the true images. Again, true pixel values are used and no boundary conditions are assumed. After adding the noise and chopping to size 256×256 for the “boat” image and size 508×508 for the “Lena” image, we obtain the observed high-resolution image \mathbf{g} . Again, we note that the pixels of \mathbf{g} are already the pixels of the low-resolution images. Therefore the image \mathbf{g} can be downsampled by a factor of 4 in

TABLE 1
The results for the 2×2 sensor array with periodic boundary condition.

Image	SNR	Least-squares model			Algorithm 2			Algorithm 3		
		PSNR	RE	β^*	PSNR	RE	β^*	PSNR	RE	Ite
Boat	30	30.00	0.0585	0.0291	32.31	0.0449	0.2596	32.34	0.0447	2
	40	30.39	0.0560	0.0275	32.67	0.0430	0.2293	32.53	0.0438	2
Lena	30	33.16	0.0421	0.0216	36.80	0.0277	0.3551	37.04	0.0270	2
	40	33.89	0.0388	0.0197	37.34	0.0261	0.2878	37.41	0.0258	2

TABLE 2
The results for the 2×2 sensor array with symmetric boundary condition.

Image	SNR	Least-squares model			Algorithm 2			Algorithm 3		
		PSNR	RE	β^*	PSNR	RE	β^*	PSNR	RE	Ite
Boat	30	32.55	0.0437	0.0173	33.82	0.0377	0.0364	34.48	0.0350	9
	40	33.88	0.0375	0.0132	34.80	0.0337	0.0239	35.23	0.0321	12
Lena	30	34.51	0.0360	0.0175	37.32	0.0261	0.0704	38.10	0.0239	6
	40	35.89	0.0308	0.0134	38.11	0.0238	0.0480	38.78	0.0221	8

both the horizontal and the vertical directions to generate the sixteen 64×64 low-resolution frames for the “boat” image and the sixteen 127×127 low-resolution frames for the “Lena” image. We emphasize that the process is the same as obtaining the low-resolution frames via (2). The vector \mathbf{g} is then used in the Tikhonov method, Algorithm 2, and Algorithm 3 to recover \mathbf{f} . Again, all three methods here make use of either the periodic or the symmetric boundary conditions to form the coefficient matrix L . The matrices L_4 , L_4^q , H_ν , and H_ν^d , $\nu = 1, 2, 3$, can be generated by the corresponding filters in Example 2, as we did in section 4.2.1.

TABLE 3
The results for the 4×4 sensor array with periodic boundary condition.

Image	SNR	Least-squares model			Algorithm 2			Algorithm 3		
		PSNR	RE	β^*	PSNR	RE	β^*	PSNR	RE	Ite
Boat	30	25.09	0.1031	0.0448	26.45	0.0882	0.2354	26.58	0.0868	3
	40	25.13	0.1026	0.0444	26.47	0.0880	0.2313	26.59	0.0867	3
Lena	30	29.42	0.0648	0.0297	31.35	0.0519	0.1918	31.55	0.0507	3
	40	29.55	0.0638	0.0297	31.41	0.0515	0.1843	31.59	0.0505	3

Tables 3 and 4 give the results of different methods. We see from the tables that the performance of Algorithm 3 is again better than that of the least-squares method and Algorithm 2 in all the cases. Figure 5 depicts the reconstructed high-resolution image with noise at SNR = 30dB for the “boat” image. As is shown in the figures, the periodic boundary condition introduces boundary artifacts in the recovered \mathbf{f} , while the symmetric one has less boundary artifacts. A comparison of Figures 5(g)–(i) reveals that Algorithm 3 gives better denoising performance than the other two methods. The recovered high-resolution images for the “Lena” image show the same result and therefore we omit them.

4.3. Super-resolution image reconstruction. In this test, we tried a partial set of the low-resolution images indexed by $A \subset \mathbb{Z}_4^2$. The following procedure is used to approximate the original high-resolution image \mathbf{f} :

Step 1: From the given partial set of low-resolution images, we apply an interpolatory subdivision scheme such as those in [6, 10] to obtain an approximate observed high-resolution image \mathbf{w} .

TABLE 4
The results for the 4×4 sensor array with symmetric boundary condition.

Image	SNR	Least-squares model			Algorithm 2			Algorithm 3		
		PSNR	RE	β^*	PSNR	RE	β^*	PSNR	RE	Ite
Boat	30	29.49	0.0621	0.0125	29.70	0.0601	0.0158	30.11	0.0579	30
	40	30.17	0.0573	0.0089	30.30	0.0566	0.0101	30.56	0.0549	45
Lena	30	32.67	0.0446	0.0147	33.49	0.0406	0.0270	34.43	0.0364	50
	40	33.43	0.0409	0.0114	33.96	0.0384	0.0188	34.73	0.0352	50

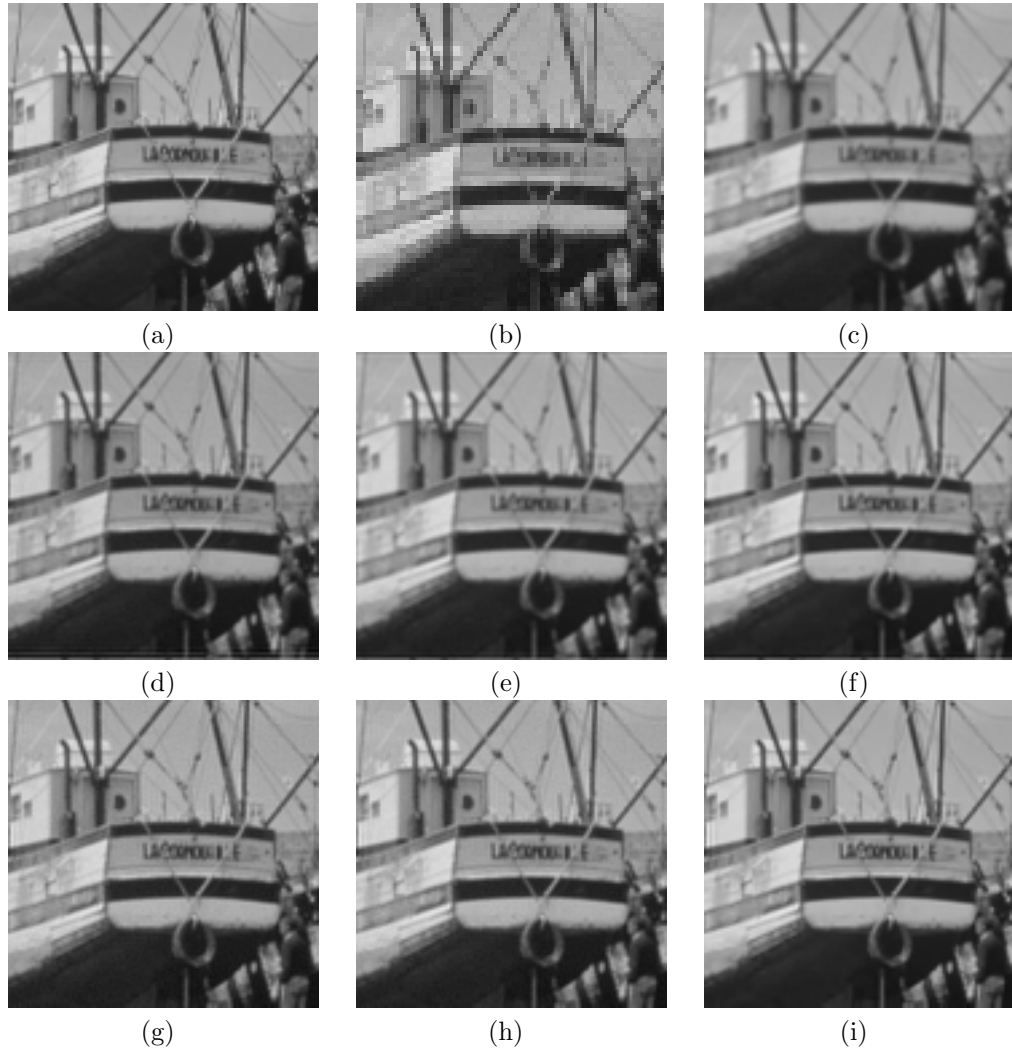


FIG. 5. (a) The original “boat” image; (b) Low-resolution 64×64 image from the $(0,0)$ th sensor; (c) Observed high-resolution 256×256 image (with white noise at $SNR=30dB$ added); (d) Reconstructed 256×256 image from the least-squares method with periodic boundary condition; (e) Reconstructed 256×256 image from Algorithm 2 with periodic boundary condition; (f) Reconstructed 256×256 image from Algorithm 3 with periodic boundary condition; (g) Reconstructed 256×256 image from the least-squares method with symmetric boundary condition; (h) Reconstructed 256×256 image from Algorithm 2 with symmetric boundary condition; (i) Reconstructed 256×256 image from Algorithm 3 with symmetric boundary condition.

- Step 2: Using \mathbf{w} as the observed high-resolution image, we solve for the high-resolution image \mathbf{u} by using the least-squares model, Algorithm 2, or Algorithm 3.
- Step 3: After obtaining \mathbf{u} , we reformulate a set of low-resolution frames from \mathbf{u} by passing it through the lowpass filter and then replacing those in the set A by the given ones. Then we have a new observed high-resolution image \mathbf{g} .
- Step 4: With this new observed high-resolution image \mathbf{g} , we solve for the final high-resolution image \mathbf{f} by using the least-squares model, Algorithm 2, or Algorithm 3.

In our test, the interpolatory filter from [6] is used in step 1 and the subset A is chosen to be $\{(0, 0), (0, 2), (1, 1), (1, 3), (2, 0), (2, 2), (3, 1), (3, 3)\}$. As in section 4.2.2, the tensor product of the lowpass filter m in Example 2 is used to generate the low-resolution images, and white noise at SNR = 40dB is added. Table 5 shows the results of the least-squares model and Algorithms 2 and 3 with symmetric boundary conditions. The optimal β^* in step 2 and step 4 is 0.0121 and 0.0105 for the least-squares method and 0.0170 and 0.0161 for Algorithm 2, respectively. The total number of iterations for Algorithm 3 in step 2 and step 4 is 35. Figure 6(a) is the approximation of the observed low-resolution image after the interpolatory subdivision scheme (i.e., it is the vector \mathbf{w} in step 1) and Figure 6(b) is the resulting picture from our super-resolution algorithm with Algorithm 3 (i.e., the vector \mathbf{f} in step 4).

TABLE 5
The results of the super-resolution image reconstruction.

Least-squares model		Algorithm 2		Algorithm 3	
PSNR	RE	PSNR	RE	PSNR	RE
27.44	0.0787	27.82	0.0753	28.03	0.0734

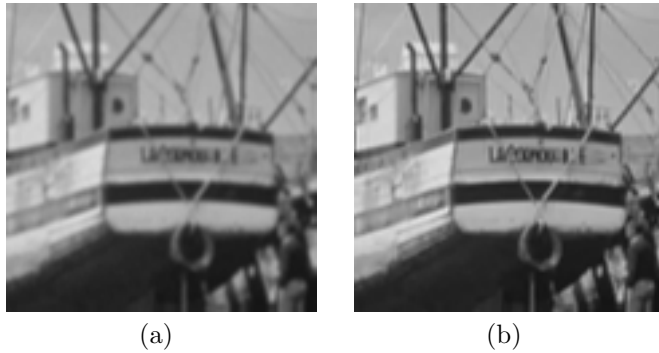


FIG. 6. (a) Approximation of the observed low-resolution image; (b) The reconstructed high-resolution image using Algorithm 3 with symmetric boundary condition.

5. Concluding remarks. Using examples in high-resolution image reconstruction, we have shown that our new wavelet thresholding algorithm is better than the traditional Tikhonov least-squares algorithm. We emphasize that the main issue here is essentially deconvolving noisy data by wavelet approach. Our new algorithm works not only for high-resolution image reconstruction but also for more general deblurring problems, as the 1D examples in section 4.1 have shown. More precisely, our

method works if, for the given low pass filter a , we can find the corresponding a^d , b_ν , and b_ν^d that satisfy (11). If it is not the case, for example, if the blurring function is a Gaussian-shaped function, one can first approximate it by a (refinable) B-spline function (or its dyadic dilation). Then, its refinement mask will be a choice of a . The dual a^d of a can be found easily (see, e.g., [5] and [10]). When a dyadic dilation of B-spline is used to approximate a Gaussian-shaped function, since a dyadic dilation of refinable B-spline is vector refinable, one can derive algorithms similar to those given here in terms of multiwavelets.

Appendix. Analysis via residuals. In this appendix, we explain through the residual analysis why (17) is the right equation to solve for the image reconstruction problem. For this, we first derive (17) by analyzing the observed function g given in (10). Since ϕ^d is refinable and since $S^1(\phi^d)$ is a half integer shift-invariant space, $\phi^d(\cdot - \alpha/2)$, $\alpha \in \mathbb{Z}^2$, are in $S^1(\phi)$. Hence, g is in $S^1(\phi^d)$ and can be written as

$$g = 2 \sum_{\alpha \in \mathbb{Z}^2} h(\alpha) \phi^d(2 \cdot -\alpha).$$

By substituting $\phi^d(\cdot)$ and its half integer translates in (10) by

$$\phi^d = 2 \sum_{\alpha \in \mathbb{Z}^2} a^d(\alpha) \phi^d(2 \cdot -\alpha)$$

and its half integer shifts, we see that $h = a^d(-\cdot) * a * v$. Therefore, the solutions of

$$(21) \quad a^d(-\cdot) * a * z = a^d(-\cdot) * a * v$$

are possible approximations of v since the given observed function g can be generated from this solution. In fact, (17) is the corresponding matrix equation for (21).

On the other hand, recovering the original image from the observed high-resolution image $a * v$ is to deconvolve the equation

$$(22) \quad a * z = a * v.$$

In fact, (4) is the matrix representation of this equation.

Here, we give some residual analysis on the difference between using (22) and (21), when only numerical approximation solutions can be obtained. Let v_1 be a numerical solution of (22) and v_2 be a numerical solution of (21). Define

$$f_1 := 2 \sum_{\alpha \in \mathbb{Z}^2} v_1(\alpha) \phi^d(2 \cdot -\alpha),$$

and

$$f_2 := 2 \sum_{\alpha \in \mathbb{Z}^2} v_2(\alpha) \phi^d(2 \cdot -\alpha).$$

Then f_1 and f_2 are the approximations of f corresponding to v_1 and v_2 . Then,

$$g_1 = \sum_{\alpha \in \mathbb{Z}^2} (a * v_1)(\alpha) \phi^d(\cdot - \alpha/2)$$

and

$$g_2 = 2 \sum_{\alpha \in \mathbb{Z}^2} (a^d(-\cdot) * a * v_2)(\alpha) \phi^d(2 \cdot -\alpha)$$

are the observed functions of f_1 and f_2 , respectively, which are the approximations of g , the observed function of f . Since only g is available, we may compare the difference between g and g_1 and also the difference between g and g_2 in terms of the residual errors of v_1 and v_2 , respectively.

Since the system $\phi^d(2 \cdot -\alpha)$, $\alpha \in \mathbb{Z}^2$, is a Riesz basis of $S^1(\phi^d)$, we will have

(23)

$$c \|a^d(-\cdot) * v - a^d(-\cdot) * a * v_2\|_2 \leq \|g - g_2\|_2 \leq C \|a^d(-\cdot) * v - a^d(-\cdot) * a * v_2\|_2.$$

The upper bound of (23) indicates that the corresponding g_2 is a good approximation of g as long as v_2 has a small residual error. The lower bound of (23) asserts that any good approximation of g must come from the solutions of (21) which have small residual errors. More precisely, let

$$f_3 := 2 \sum_{\alpha \in \mathbb{Z}^2} v_3(\alpha) \phi^d(2 \cdot -\alpha)$$

be an arbitrary approximate solution of f , and g_3 be the corresponding observed function. The lower bound estimate of (23) asserts that $\|a^d(-\cdot) * v - a^d(-\cdot) * a * v_3\|_2$ must be small if $\|g - g_3\|_2$ is small.

On the other hand, since the system $\phi^d(\cdot - \alpha/2)$, $\alpha \in \mathbb{Z}^2$, normally is not a Riesz system (only the upper Riesz bound in (8) holds for this system), we have only

$$(24) \quad \|g - g_1\|_2 \leq C \|a * v - a * v_1\|_2.$$

This indicates that those solutions of (22) with small residual errors will have their observed function close to g . However, the lack of lower bound estimate for (24) indicates that not all good approximations of g necessarily come from the solutions of (22) with small residual errors.

REFERENCES

- [1] N. BOSE AND K. BOO, *High-resolution image reconstruction with multisensors*, International J. Imaging Systems and Technology, 9 (1998), pp. 294–304.
- [2] C. BRISLAWN, *Classification of nonexpansive symmetric extension transforms for multirate filter banks*, Appl. Comput. Harmon. Anal., 3 (1996), pp. 337–357.
- [3] D. CAPEL AND A. ZISSERMAN, *Super-resolution enhancement of text image sequences*, in Proceedings of the International Conference on Pattern Recognition, International Association for Pattern Recognition, Vol. 1, 2000.
- [4] R. COIFMAN AND D. DONOHO, *Wavelet and Statistics*, Lecture Notes in Statist. 103, Springer-Verlag, New York, 1994, pp. 125–150.
- [5] I. DAUBECHIES, *Ten Lectures on Wavelets*, CBMS–NSF Regional Conf. Ser. in Appl. Math., 61, SIAM, Philadelphia, 1992.
- [6] G. DESLAURIERS AND S. DUBUC, *Symmetric iterative interpolation processes*, Constr. Approx., 5 (1989), pp. 49–68.
- [7] D. DONOHO, *De-noising by soft-thresholding*, IEEE Trans. Inform. Theory, 41 (1995), pp. 613–627.
- [8] H. ENGL, M. HANKE, AND A. NEUBAUER, *Regularization of Inverse Problems*, Kluwer Academic Publishers, Dordrecht, The Netherlands, 1996.
- [9] R. GONZALEZ AND R. WOODS, *Digital Image Processing*, Addison–Wesley, Reading, MA, 1993.
- [10] H. JI, S. RIEMENSCHNEIDER, AND Z. SHEN, *Multivariate compactly supported fundamental refinable functions, dual and biorthogonal wavelets*, Stud. Appl. Math., 102 (1999), pp. 173–204.
- [11] S. JEFFERIES AND J. CHRISTOU, *Restoration of astronomical images by iterative blind deconvolution*, Astrophysics J., 415 (1993), pp. 862–874.
- [12] J. KALIFA AND S. MALLAT, *Thresholding estimators for inverse problems and deconvolutions*, Ann. Statist., submitted, also available online from <http://www.cmap.polytechnique.fr/~mallat>.

- [13] J. KALIFA, S. MALLAT, AND B. ROUG, *Minimax deconvolution in mirror wavelet bases*, IEEE Trans. Image Process, submitted; also available online from <http://www.cmap.polytechnique.fr/~mallat>.
- [14] E. KALTENBACHER AND R. HARDIE, *High resolution infrared image reconstruction using multiple, low resolution, aliased frames*, in Proceedings of IEEE 1996 National Aerospace and Electronic Conference, IEEE Computer Society Press, Piscataway, NJ, 1996, pp. 702–709.
- [15] S. KIM, N. BOSE, AND H. VALENZUELA, *Recursive reconstruction of high resolution image from noisy undersampled multiframe*, IEEE Trans. Acoust., Speech, and Signal Process., 38 (1990), pp. 1013–1027.
- [16] W. LAWTON, S. L. LEE, AND Z. SHEN, *Stability and orthonormality of multivariate refinable functions*, SIAM J. Math. Anal., 28 (1997), pp. 999–1014.
- [17] S. MALLAT, *A Wavelet Tour of Signal Processing*, 2nd ed., Academic Press, San Diego, CA, 1999.
- [18] M. K. NG, R. H. CHAN, AND W. C. TANG, *A fast algorithm for deblurring models with Neumann boundary conditions*, SIAM J. Sci. Comput., 21 (1999), pp. 851–866.
- [19] W. RUDIN, *Real and Complex Analysis*, McGraw-Hill, New York, 1987.
- [20] Z. SHEN, *Extension of matrices with Laurent polynomial entries*, in Proceedings of the 15th IMACS World Congress 1997 on Scientific Computation, Modelling and Applied Mathematics, A. Syclow, ed., 1997, pp. 57–61.
- [21] S. SKIENA, *The Algorithm Design Manual*, Springer-Verlag, Berlin, 1997.
- [22] R. SCHULTZ AND R. STEVENSON, *Extraction of high-resolution frames from video sequences*, IEEE Trans. Image Process., 5 (1996), pp. 996–1011.
- [23] A. TEKALP, M. OZKAN, AND M. SEZAN, *High-resolution image reconstruction from lower-resolution image sequences and space-varying image restoration*, in Proceedings of the IEEE International Conference on Acoustics, Speech, and Signal Processing, Vol. III, IEEE Press, Piscataway, NJ, 1992, pp. 169–172.
- [24] R. TSAI AND T. HUANG, *Multiframe image restoration and registration*, Advances in Computer Vision and Image Processing, 1 (1984), pp. 317–339.
- [25] M. V. WICKERHAUSER, *Adapted Wavelet Analysis from Theory to Software*, A. K. Peters, Boston, MA, 1994.